



OGLE-2014-BLG-0962 and a Comparison of Galactic Model Priors to Microlensing Data

Yutong Shan¹, Jennifer C. Yee^{1,23} , Andrzej Udalski^{2,24}, Ian A. Bond^{3,25}, Yossi Shvartzvald^{4,26} , In-Gu Shin¹ ,
Youn-Kil Jung¹ , Sebastiano Calchi Novati⁵ , Charles A. Beichman⁶, Sean Carey⁷ , B. Scott Gaudi⁸ , Andrew Gould⁸,
Richard W. Pogge⁸

(The Spitzer Team),

Radosław Poleski^{8,9} , Jan Skowron⁹ , Szymon Kozłowski⁹ , Przemysław Mróz² , Paweł Pietrukowicz² ,
Michał K. Szymański², Igor Soszyński² , Krzysztof Ulaczyk² , Łukasz Wyrzykowski²

(The OGLE Collaboration),

Fumio Abe¹⁰, Richard K. Barry¹¹, David P. Bennett^{11,12} , Aparna Bhattacharya^{11,12}, Martin Donachie¹³, Akihiko Fukui¹⁴ ,
Yuki Hirao¹⁵, Yoshitaka Itow¹⁰ , Kohei Kawasaki¹⁵ , Iona Kondo¹⁵, Naoki Koshimoto^{16,17} , Man Cheung Alex Li¹³,
Yutaka Matsubara¹⁰, Yasushi Muraki¹⁰, Shota Miyazaki¹⁵ , Masayuki Nagakane¹⁵, Clément Ranc¹¹ ,
Nicholas J. Rattenbury¹³ , Haruno Suematsu¹⁵, Denis J. Sullivan¹⁸, Takahiro Sumi¹⁵, Daisuke Suzuki¹⁹ , Paul J. Tristram²⁰,
Atsunori Yonehara²¹

(The MOA Collaboration),

and

Dan Maoz²², Shai Kaspi²², and Matan Friedmann²²

(The Wise Group)

¹ Harvard-Smithsonian Center for Astrophysics, 60 Garden Street, Cambridge, MA 02138, USA; yshan@cfa.harvard.edu

² Warsaw University Observatory, Al. Ujazdowskie 4, 00-478 Warszawa, Poland

³ Institute of Natural and Mathematical Sciences, Massey University, Auckland 0745, New Zealand

⁴ Jet Propulsion Laboratory, California Institute of Technology, 4800 Oak Grove Drive, Pasadena, CA 91109, USA

⁵ IPAC, Mail Code 100-22, Caltech, 1200 E. California Blvd., Pasadena, CA 91125, USA

⁶ NASA Exoplanet Science Institute, MS 100-22, California Institute of Technology, Pasadena, CA 91125, USA

⁷ Spitzer Science Center, MS 220-6, California Institute of Technology, Pasadena, CA, USA

⁸ Department of Astronomy, Ohio State University, 140 W. 18th Ave., Columbus, OH 43210, USA

⁹ Warsaw University Observatory, Al. Ujazdowskie 4, 00-478 Warszawa, Poland

¹⁰ Institute for Space-Earth Environmental Research, Nagoya University, Nagoya 464-8601, Japan

¹¹ Code 667, NASA Goddard Space Flight Center, Greenbelt, MD 20771, USA

¹² Department of Astronomy, University of Maryland, College Park, MD 20742, USA

¹³ Department of Physics, University of Auckland, Private Bag 92019, Auckland, New Zealand

¹⁴ Okayama Astrophysical Observatory, National Astronomical Observatory of Japan, 3037-5 Honjo, Kamogata, Asakuchi, Okayama 719-0232, Japan

¹⁵ Department of Earth and Space Science, Graduate School of Science, Osaka University, Toyonaka, Osaka 560-0043, Japan

¹⁶ Department of Astronomy, Graduate School of Science, The University of Tokyo, 7-3-1 Hongo, Bunkyo-ku, Tokyo 113-0033, Japan

¹⁷ National Astronomical Observatory of Japan, 2-21-1 Osawa, Mitaka, Tokyo 181-8588, Japan

¹⁸ School of Chemical and Physical Sciences, Victoria University, Wellington, New Zealand

¹⁹ Institute of Space and Astronautical Science, Japan Aerospace Exploration Agency, 3-1-1 Yoshinodai, Chuo, Sagami-hara, Kanagawa, 252-5210, Japan

²⁰ University of Canterbury Mt. John Observatory, P.O. Box 56, Lake Tekapo 8770, New Zealand

²¹ Department of Physics, Faculty of Science, Kyoto Sangyo University, 603-8555 Kyoto, Japan

²² School of Physics and Astronomy and Wise Observatory, Tel-Aviv University, Tel-Aviv 6997801, Israel

Received 2018 May 23; revised 2019 January 15; accepted 2019 January 17; published 2019 February 28

Abstract

OGLE-2014-BLG-0962 (OB140962) is a stellar binary microlensing event that was well covered by observations from the *Spitzer* satellite as well as ground-based surveys. Modeling yields a unique physical solution: a mid-M +M-dwarf binary with $M_{\text{prim}} = 0.20 \pm 0.01 M_{\odot}$ and $M_{\text{sec}} = 0.16 \pm 0.01 M_{\odot}$, with projected separation of 2.0 ± 0.3 au. The lens is only $D_{LS} = 0.41 \pm 0.06$ kpc in front of the source, making OB140962 a bulge lens and the most distant *Spitzer* binary lens to date. In contrast, because the Einstein radius ($\theta_E = 0.143 \pm 0.007$ mas) is unusually small, a standard Bayesian analysis, conducted in the absence of parallax information, would predict a brown dwarf binary. We compare the results of Bayesian analysis using two commonly used Galactic model priors to the measured values for a set of *Spitzer* lenses. We find all models tested predict lens properties consistent with the *Spitzer* data. Furthermore, we illustrate the methodology for probing the Galactic distribution of planets by comparing the cumulative distance distribution of the *Spitzer* two-body lenses to that of the *Spitzer* single lenses.

Key words: binaries: general – Galaxy: bulge – gravitational lensing: micro – methods: statistical – stars: low-mass

1. Introduction

Gravitational microlensing is a type of transient phenomenon in which a temporary alignment of a foreground lens and a background source causes the source to be magnified. Because lensing is sensitive to the presence of mass independent of any

²³ The *Spitzer* Team.

²⁴ The OGLE Collaboration.

²⁵ The MOA Collaboration.

²⁶ The Wise Group.

associated flux, it represents a unique means to probe distant and faint populations of many compact astrophysical objects of interest (e.g., low-mass main-sequence stars, brown dwarfs, planets, and stellar remnants). Indeed, microlensing has discovered stellar remnants (e.g., Shvartzvald et al. 2015; Wyrzykowski et al. 2016) and candidate free-floating planets (e.g., Sumi et al. 2011; Mróz et al. 2017, 2018), as well as characterized planets and low-mass objects anywhere between the Sun and the Galactic center.

One drawback of the microlensing technique is that, while relative parameters such as mass ratios (for two-body lenses) are routinely measured, it is often difficult to infer the absolute physical properties of the lens from a ground-based light curve alone. For many applications, the absolute physical properties of the lens—its mass (M_L), distance (D_L), and lens–source relative kinematics (v_{rel})—are paramount to interpretation. For example, in characterizing individual lensing systems, uncertainty in the physical parameters can make the difference between a star, a brown dwarf, a planet, or a moon (e.g., Bennett et al. 2014; Albrow et al. 2018). To study the distribution of planet masses from an ensemble of binary lens mass ratios (Shvartzvald et al. 2016b; Suzuki et al. 2016), the host masses are needed. Measurement of planetary occurrence rate as a function of distance and Galactic environment (e.g., Penny et al. 2016) also depends on whether the system distances and kinematic memberships are reliably assigned on average.

The challenge of determining physical quantities for lenses from ground-based data alone arises because four parameters are needed to constrain the four physical properties (that is, two scalar quantities, M_L and D_L , and one vector quantity with two components, $v_{\text{rel}} = [v_{\text{rel,N}}, v_{\text{rel,E}}]$). The microlensing parameters t_E (Einstein timescale), θ_E (Einstein radius), and π_E (microlensing parallax) form a complete set that can be solved for the physical parameters (see Section 3.1). However, only t_E is readily measured for microlensing events. One can measure θ_E using the finite-source effect, which is not usually present for single-lens events but often feasible for binary lensing. This leaves π_E , which, prior to *Spitzer*, was not accessible for most events because their t_E is considerably less than 1 yr.

In most cases for which π_E is not available, a Bayesian analysis can be used to obtain a posterior on the physical properties of a particular event. This is done by forward-modeling individual source and lens stars in the Galaxy to match with the measured t_E and θ_E of the event. The priors for such a model integrate kinematics, stellar density profiles, and mass functions for the Galactic disk and bulge. Since most microlensing events will have ground-based survey data only, Bayesian analysis will continue to be the leading avenue used to estimate the physical parameters of microlensing systems, until the *Wide Field Infrared Survey Telescope (WFIRST)*; Spergel et al. 2013) era.

Given the importance of physical parameters for the correct interpretation of lensing systems, it would be useful to examine the accuracy of Bayesian analysis. One test would be to compare the Bayesian predictions to the “true” values determined from other means, available for a small (but growing) number of systems. One way to arrive at the “true” answers is to perform follow-up adaptive optics (AO) imaging, specifically to resolve the source and lens separately. Notably, AO solutions were obtained in a handful of cases, finding generally good agreement with the original Bayesian predictions. For example, Batista et al. (2014) found the host mass and distance of MOA-2011-BLG-293

to be $M_L = 0.86 \pm 0.06 M_\odot$ and $D_L = 7.72 \pm 0.44$ kpc, fully consistent with the Bayesian predictions of $M_L = 0.59^{+0.35}_{-0.29} M_\odot$ and $D_L = 7.15 \pm 0.75$ kpc (Yee et al. 2012). For OGLE-2005-BLG-169, Bennett et al. (2015) and Batista et al. (2015) retrieve physical properties ($M_L = 0.69 \pm 0.02 M_\odot$ and $D_L = 4.1 \pm 0.4$ kpc) consistent with the original Bayesian result from Gould et al. (2006, $M_L = 0.49^{+0.23}_{-0.29} M_\odot$ and $D_L = 2.7^{+1.6}_{-1.3}$ kpc). Of course, the Bayesian constraints are quite broad, so their consistency with the true answers in a handful of cases does not necessarily confirm their overall accuracy. The Bayesian analysis is also not unique: each applies a particular set of Galactic model priors. Therefore, determining whether Bayesian analysis is accurate or could be systematically biased, as well as the extent to which the inferred properties are affected by model assumptions, would require a larger lens sample for comparison to a representative set of typical Galactic model priors.

Augmenting the sample of well-characterized lens systems has recently been made possible by satellite microlensing, as simultaneous observation by a distant satellite provides another way to obtain the “true” parameters of a microlensing event. Since microlensing events involve very precise alignment between the lens system and the source star trajectory, the alignment angle is different for two widely separated observers, leading to inter-light curve discrepancies that can be modeled to yield π_E . This principle motivated the *Spitzer* microlensing campaign, which, since its inaugural year in 2014, has yielded numerous parallax measurements to single lenses (e.g., Calchi Novati et al. 2015a; Yee et al. 2015b; Zhu et al. 2017). Moreover, *Spitzer* has helped to measure π_E for a dozen stellar binaries (e.g., Bozza et al. 2016; Han et al. 2017; Wang et al. 2017) and planets (e.g., Udalski et al. 2015b; Street et al. 2016; Shvartzvald et al. 2017; Ryu et al. 2018), disentangling the absolute physical properties of the lens systems.

The *Spitzer* microlensing campaign adds to the set of microlensing systems with well-constrained properties, and these systems form an ideal test bed for Bayesian analysis. At least two *Spitzer* objects have published Bayesian analysis results. The physical properties of the single-lens OB151482 found by detailed modeling of the finite source effect (Chung et al. 2017) yielded a mass and distance consistent with a Bayesian analysis presented by Zhu et al. (2017) for the same object. However, for the low-mass-ratio planet OB161195, the Bayesian predictions by Bond et al. (2017) are in tension with the parameters found by a full modeling including the *Spitzer* light curve presented in Shvartzvald et al. (2017).

A systematic comparison of the Bayesian method to the true measurements would also test the underlying Galactic model priors. The Bayesian analysis is a prediction of the observations based on a particular Galactic model. If there are systematic differences between the Bayesian results and measurements, this could reflect a need to adjust the Galactic model priors. Such a test would complement other direct tests of models of the Galaxy, such as comparisons to star counts (e.g., Penny et al. 2013, 2018) or the microlensing event rate and optical depth (e.g., Han & Gould 1995b; Sumi et al. 2013; Awiphan et al. 2016).

This work presents the discovery of OGLE-2014-BLG-0962 (OB140962), a textbook example of a stellar binary lens with excellent data coverage from both the ground and *Spitzer*, leading to superbly constrained physical parameters. We describe the data in Section 2 and the modeling process in

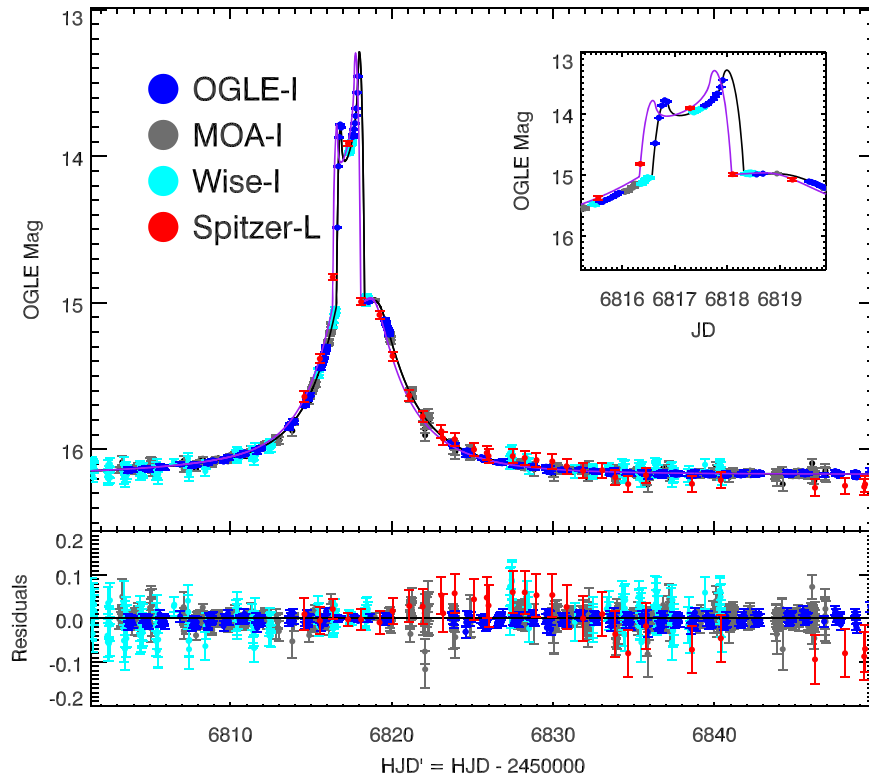


Figure 1. Ground- and space-based light curves of binary microlensing event OGLE-2014-BLG-0962, including data from OGLE, MOA, Wise, and *Spitzer*. The best-fit $u_0 > 0$ model is shown in black, while the purple curve outlines the corresponding space-based solution. The inset shows a zoom-in of the highly magnified portion.

Section 3. In particular, we give the mathematical relations between the microlensing and physical parameters of interest in Section 3.1. The unique physical properties for this lens are given in Section 4, where we find that this binary is likely the most distant stellar binary detected by *Spitzer* to date, and very likely a member of the Galactic bulge.

In Section 5 we start by performing Bayesian analysis on OB140962 while withholding the parallax information (Section 5.2). We subsequently repeat this analysis for other *Spitzer* events with secure parallax-derived physical parameters to investigate the overall reliability of Bayesian analysis and compare the effects of varying the Galactic model priors.

Finally, in Section 6, we compare the distance distribution of well-characterized *Spitzer* binaries (including planets) to that of the *Spitzer* single lenses. This serves to illustrate how one might quantify the relative occurrence rate of planets and binaries throughout the Galaxy when a larger sample becomes available and selection effects are systematically quantified. Section 7 provides a summary.

2. Observations

OGLE-2014-BLG-0962 (hereafter OB140962) was located at equatorial coordinates $(\alpha, \delta)_{J2000} = (18:01:42.98, -27:55:56.2)$. These translate into Galactic coordinates $(l, b) = (2^\circ 7', -2^\circ 5')$. It was alerted by the Optical Gravitational Lensing Experiment Early Warning System (OGLE; Udalski et al. 2015a; EWS: Udalski 2003) at UT 18:53, 2014 May 30, in time to mobilize immediate follow-up observations by the first *Spitzer* microlensing campaign (e.g., Udalski et al. 2015b; Yee et al. 2015a). The light curve, as shown in Figure 1, is a caustic crossing event that reveals a clear signature of a high-mass-ratio binary lens. The

caustic entrance and exit are well covered by both ground- (Section 2.1) and space-based (Section 2.2) observations, leading to secure determination of microlensing and physical lens parameters. Prior to modeling, the errors on the photometric reduction from each observatory were rescaled according to standard procedures and clipped for outliers (Section 2.3).

2.1. Ground-based Observations

The OGLE observations are conducted with the 1.3 m Warsaw telescope at the Las Campanas Observatory in Chile, with a 1.4 deg^2 field of view (FOV) camera. Data in the *I* band were taken at a nominal cadence of $\Gamma = 1 \text{ hr}^{-1}$. The regions around and between the caustic crossings are well sampled. *V*-band data were also acquired at a lower cadence. Four points, including one near peak, were captured in the OGLE *V* band between $\text{HJD}' = 6810$ and 6830. OGLE photometry was reduced with the difference-imaging analysis (DIA) method (Alard & Lupton 1998; Wozniak 2000).

The Microlensing Observations in Astrophysics (MOA) collaboration also observed this event (MOA-2014-BLG-285). MOA provided an alert on 2014 May 31. The MOA survey is conducted from the University of Canterbury Mt. John Observatory in New Zealand, which features a 1.8 m telescope with a camera whose FOV is 2.2 deg^2 . MOA observes in the custom R_{MOA} band, which is approximately the superposition of the standard *I* and *R* bands. Normally MOA surveys at high cadence, though for this particular event it missed the portion of the light curve between the caustic entrance and exit because of weather. MOA photometry is reduced by the DIA pipeline summarized in Bond et al. (2001).

Table 1
Error Rescaling Factors for Each Observatory

Observatory	k
OGLE	See Skowron et al. (2016)
MOA	1.25
Wise	1.46
<i>Spitzer</i>	7.9

The Wise microlensing survey (Shvartzvald et al. 2016b) used the 1 m telescope at Tel Aviv University’s Wise Observatory in Israel. The Large Area Imager for the Wise Observatory camera (with FOV = 1 deg²) was used to collect data on this event in survey mode. Wise observations are conducted in the *I* filter. The nominal cadence is 30 minutes, averaging five to six observations per night because of target visibility. Photometry for Wise is performed with the DIA software described in Albrow et al. (2009).

2.2. Space-based Observations

OB140962 was observed in the first season of the *Spitzer* microlensing campaign, before the development of the objective target selection procedure of Yee et al. (2015a), which was used in subsequent seasons. *Spitzer* observations were taken in the *L* band (3.6 μ m). The target was selected for *Spitzer* observations before it showed any features attributable to a binary. Observations began on 2014 June 6 (HJD’ = 6814.59). The last data point was taken on 2014 July 10 (HJD’ = 6849.34). A total of 31 observations were taken at a cadence of $\Gamma \sim 1 \text{ day}^{-1}$. It captured several points during the anomaly. *Spitzer* photometry was reduced with the pipeline presented in Calchi Novati et al. (2015b).

2.3. Error Rescaling

Purely photometric (i.e., Poisson) errors are often underestimated, which prompts a rescaling of the data points and renormalization of the errors. Except for the OGLE errors, which are rescaled based on the recommended procedure of Skowron et al. (2016), errors from the other observatories (in magnitudes) are modified using the scheme of Yee et al. (2012),²⁷ where

$$\sigma_{\text{rescaled}} = k\sigma_{\text{pipeline}}. \quad (1)$$

With σ_{rescaled} , every data point should contribute ~ 1 in χ^2 on average. The k factor is adjusted manually until this is the case. The newly scaled errors are used to reject outliers and updated iteratively. As a result, we reject four OGLE, two MOA, and two Wise measurements. The final adopted k parameters are listed in Table 1.

3. Analysis

In this section, we deduce the microlensing parameters and physical lens properties via joint modeling of the ground- and space-based light curves. In Section 3.1 we introduce the relevant parameters that can be measured from our data and describe how to use them to obtain the absolute physical properties. But even prior to rigorous modeling, many conclusions can be drawn from the data points alone thanks

to the comprehensive coverage of the event from both the ground and space. Therefore, in Section 3.2 we provide a heuristic description of the light curve, which yields basic insight into the nature of the microlensing event. Section 3.3 summarizes the multistage modeling process to eventually arrive at the microlensing parameters.

3.1. Microlensing Parameters and Relations to Physical Properties

Six fundamental parameters are associated with and routinely measured for binary lensing light curves: (t_0 , u_0 , t_E , s , q , α). The first three quantities stand for the peak time, impact parameter of the source trajectory to the lens (scaled to the lens Einstein radius, θ_E ; see below), and the Einstein timescale, that is, the characteristic width of the portion of the light curve undergoing magnification. The second set of three parameters pertains to the binary lens. They are the instantaneous projected separation between the components (normalized to θ_E), their mass ratio, and the projected angle of the source trajectory to the binary axis, respectively.

All of the parameters presented so far are either geometric or relative. Of course, it is the absolute physical properties of the lens that are of greatest interest. The lens mass (M_L), distance (D_L), and relative proper motion between the lens and source (μ_{rel}) can be determined provided additional effects are measured. They are linked to the direct observables via the Einstein radius (θ_E) and the dimensionless vector microlensing parallax (π_E). For $\pi_{\text{rel}} \equiv \pi_L - \pi_S = \text{au}(D_L^{-1} - D_S^{-1})$, D_S being the source distance (usually close to the Galactic center at ~ 8.3 kpc), θ_E and π_E are defined as follows (e.g., Gould 2000):

$$\theta_E \equiv \sqrt{\kappa M_L \pi_{\text{rel}}}; \quad \kappa \equiv \frac{4G}{c^2 \text{au}} \approx 8.14 \text{ mas } M_\odot^{-1}; \quad (2)$$

and

$$\pi_E \equiv \frac{\pi_{\text{rel}} \mu_{\text{rel}}}{\theta_E |\mu_{\text{rel}}|}; \quad \mu_{\text{rel}} = \frac{\theta_E}{t_E}. \quad (3)$$

Manipulating Equations (2) and (3), we find that both the lens mass and distance can be expressed as a function of θ_E and π_E :

$$M_L = \frac{\theta_E}{\kappa \pi_E}; \quad D_L = \frac{\text{au}}{\pi_E \theta_E + \text{au}/D_S}. \quad (4)$$

For caustic crossing events, the finite source effect constrains a seventh parameter ρ , where

$$\rho \equiv \frac{\theta_\star}{\theta_E} = \frac{t_\star}{t_E}, \quad (5)$$

that is, the size of the source θ_\star measured in units of θ_E . If the source radius can be deduced independently, for instance from the event’s position in the local color–magnitude diagram (CMD), then θ_E can be calculated. Alternatively, ρ can be defined as the source self-crossing time, t_\star , relative to t_E .

The microlensing parallax, π_E , can be measured with a second line of sight to the event, which generally will result in a light curve with timing and morphology that are distinct from the first because of the apparent difference in trajectory. A useful qualitative approximation for the components of π_E is given by the scaled difference in t_0 and u_0 between the two

²⁷ The original formulation is $\sigma_{\text{rescaled}} = k\sqrt{\sigma_{\text{pipeline}}^2 + \sigma_{\text{min}}^2}$, though, in many cases including this one, $\sigma_{\text{min}} \approx 0$.

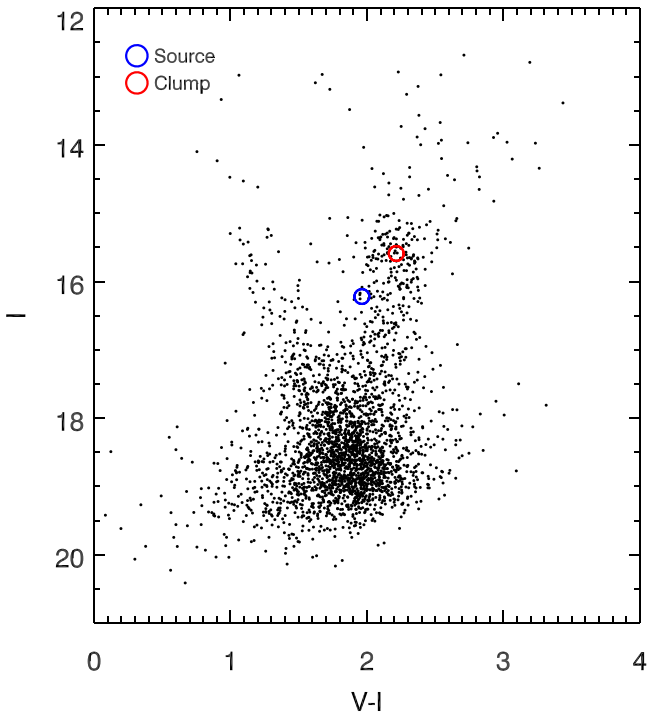


Figure 2. The local color–magnitude diagram around OB140962. The red giant clump centroid is located at the center of the red circle.

sight lines (e.g., Refsdal 1966):

$$\pi_E = \frac{\text{au}}{D_\perp} \left(\frac{\Delta t_0}{t_E}; \Delta u_0 \right) \quad (6)$$

where D_\perp is the projected separation vector between the two observing locations in the plane of the sky. Equation (6) applies for the coordinate system in which the x axis is aligned with D_\perp . For Earth and the *Spitzer* satellite, the magnitude of this vector is approximately 1–1.5 au. Refer to, for example, Equations (8) to (10) in Calchi Novati et al. (2015a) for the exact relation between π_E , Δt_0 , Δu_0 , and instantaneous D_\perp , which is used in the actual modeling for π_E .

3.2. Heuristic Description of the Light Curve

The ground-based light curve has a broad double-horned structure characteristic of roughly equal mass-ratio binary lensing, exhibiting a clear caustic entrance ($\text{HJD}' = \text{HJD} - 2450000 \sim 6816.6$) and exit ($\text{HJD}' \sim 6818.3$). The hump in the light curve immediately following the caustic exit ($\text{HJD}' \sim 6819.0$) implies a cusp approach. The shape and timing of these features place tight constraints on the event geometry. Below we illustrate the back-of-the-envelope process of converting the light curve components into microlensing parameters and interpret the inferred physical properties of the source–lens system.

We approximate this event to have zero blending and estimate the Einstein timescale (t_E) from the half-width of the magnified portion of the light curve at $1.3\times$ the baseline flux. For this event, $t_E \sim 5$ days. The caustic crossings resolve the source size (i.e., finite source effect), allowing us to determine θ_E from Equation (5). Figure 1 shows the half-width of the caustic entrance is $t_x \sim 0.15$ day, so $\rho \approx 0.03$. To obtain θ_* , we note that the event placement in the local CMD is consistent

with a bulge giant (Figure 2 and Section 4.1). A typical clump giant might have a radius $5\text{--}10\times$ that of the Sun, say $\theta_* \approx 4 \mu\text{as}$. Then, $\theta_E \approx 0.13$ mas. Together with t_E and Equation (3), we find that the relative lens–source proper motion is $\mu_{\text{rel}} \approx 9.5 \text{ mas yr}^{-1}$.

For many microlensing discoveries with only ground-based data, deducing θ_E and μ_{rel} is as far as we can go. To estimate the absolute physical properties of the lens, we might assume the lens has a typical distance of $D_L \sim 6$ kpc. Assuming a source distance of $D_S \sim 8.3$ kpc, $\pi_{\text{rel}} \approx 0.046$. Then, substituting $\theta_E \approx 0.13$ mas into Equation (2) gives $M_{\text{tot}} \approx 0.045 M_\odot$. Therefore, the atypically small θ_E for this event (normally ~ 0.5 mas) implies an exciting low-mass brown dwarf (BD)–BD binary.

For this event we have parallax information, which constrains the true lens distance and mass. To estimate π_E , we see from Equation (6) that $|\pi_E| \approx \sqrt{(\Delta t_0/t_E)^2 + (\Delta u_0)^2}$, where we have used the fact that D_\perp is of order 1 au. For OB140962, the *Spitzer* light curve actually closely mimics the ground-based one in shape as well as timing, but offset by $\Delta t_0 \sim 0.3$ day. The virtually indistinguishable light curve morphologies between the two sight lines strongly imply nearly identical impact parameters between the two events (i.e., Δu_0 is negligible), so $\pi_E \sim \Delta t_0/t_E \approx 0.06$. The physical parameters M_{tot} and D_L can both be computed from θ_E and π_E . According to Equation (4), $M_{\text{tot}} \approx 0.27 M_\odot$ and $D_L \approx 7.8$ kpc. Here we have again assumed that the source is located at the Galactocentric distance $R_0 \sim 8.3$ kpc. Therefore, from this heuristic evaluation of the ground light curves in conjunction with the *Spitzer* parallax, we reach the conclusion that the lens is a typical low-mass binary that must be very close to the source. This is at odds with the earlier expectation of a very low mass lens from θ_E and μ_{rel} alone.

3.3. Modeling the Light Curve

To map the overall topology of the parameter space for the ground-based light curve, we perform a grid search in χ^2 space over $\log s$, $\log q$, and α , which are responsible for the magnification profile of the event (Dong et al. 2006). For each point ($\log s \in [-1, 1]$, $\log q \in [-5, 1]$, $\alpha \in [0, 2\pi]$) on the $100 \times 100 \times 21$ grid, we allow the other light curve parameters (t_0 , u_0 , t_E , ρ) to be explored by a Markov chain Monte Carlo (MCMC) algorithm until it settles on the minimal χ^2 . We find the global minimum χ^2 to be in the region around $\log s \sim 0.3$ and $\log q \sim 0.07$ (based on modeling the OGLE *I*-band data prior to error rescaling).

From the best-fit grid point, we launch our full MCMC for a joint fit for all four data sets (three ground, one space). The finite source effect is modeled using the ray-shooting method (Kayser et al. 1986; Schneider & Weiss 1986; Wambsganss 1997), and regions of the light curve immediately adjacent to caustic crossings are computed through the hexadecapole approximation (Gould 2008; Pejcha & Heyrovský 2009). With the inclusion of the space data, two additional parameters associated with the space parallax are fit: $\pi_E = (\pi_{E,N}, \pi_{E,E})$. We modeled the limb darkening of the source star using the parameters derived in Section 4.1. The final best-fit solutions are compiled in Table 2. The parameter errors presented are 16% and 84% confidence intervals (CIs), evaluated from the MCMC posteriors.

Single-lens satellite parallax suffers from the well-known four-fold degeneracy (e.g., Refsdal 1966; Gould 1994). For binary lensing, depending on the data quality and coverage,

Table 2
Posterior and Best-fit Microlensing Parameters Combining Ground and Space Observations

Model	χ^2_{total}	$t_0 - 6817$ (HJD')	u_0	t_E (days)	$\log(s)$	$\log(q)$	α (rad)	ρ	$\pi_{E,N}$	$\pi_{E,E}$	$f_{s,OGLE}$	$f_{b,OGLE}$
$u_0 > 0$ Median	...	0.5469	0.0039	6.454	0.2782	-0.103	-4.183	0.0240	0.0079	0.0480	5.05	0.34
68% CI (Upper)	...	0.0018	0.0007	0.032	0.0012	0.005	0.004	0.0002	0.0023	0.0008	0.04	0.04
68% CI (Lower)	...	-0.0018	-0.0007	-0.032	-0.0012	-0.005	-0.004	-0.0002	-0.0030	-0.0007	-0.04	-0.04
Best-fit	6847.596	0.5469	0.0038	6.482	0.2787	-0.105	-4.182	0.0239	0.0091	0.0477	5.02	0.37
$u_0 < 0$ Median	...	0.5474	-0.0039	6.455	0.2782	-0.104	4.183	0.0240	0.0038	0.0484	5.05	0.34
68% CI (Upper)	...	0.0018	0.0007	0.032	0.0011	0.005	0.004	0.0002	0.0030	0.0006	0.04	0.03
68% CI (Lower)	...	-0.0018	-0.0007	-0.031	-0.0011	-0.005	-0.004	-0.0002	-0.0023	-0.0006	-0.04	-0.04
Best-fit	6847.872	0.5469	-0.0039	6.465	0.2782	-0.106	4.182	0.0239	0.0029	0.0482	5.03	0.36

Note.

DoF = 7570-11.

some degeneracies can be resolved (see discussion in, e.g., Zhu et al. 2015). The light curve of OB140962 is well covered from both the ground and space, leading to a straightforward interpretation. In this case, the $u_0 > 0$ and $u_0 < 0$ degeneracy persists but maps into nearly identical physical properties. Therefore, the physical solution is unique. In Figure 1 we plot the $u_0 > 0$ solution based on the corresponding best-fitting parameters. Figure 3 shows the associated caustic structure.

A comparison between the final fitted microlensing parameters and those from the heuristic assessment of Section 3.2 reveals that they are qualitatively consistent.

We also fit for higher-order effects in the OGLE I -band light curve, but we found that no meaningful constraints could be placed on the annual parallax and orbital motion from these data alone. This is unsurprising because these phenomena typically manifest on timescales of tens to hundreds of days. In contrast, OB140962 is magnified for merely ~ 10 days, with only ~ 2 days between caustic crossings.

4. Properties of the Source and Lens

4.1. Source Star Limb Darkening and Angular Radius

The source star properties can be inferred from its position on the local CMD. We calculate the apparent source ($V-I$) color by fitting a line to the observed event flux in the OGLE V versus OGLE I bands. This yields a model-independent color of $(V-I) = 1.963 \pm 0.006$. Modeling the source flux yields an apparent I -band magnitude of 16.22 ± 0.01 .

Using the observed ($V-I$) versus I CMD from OGLE in the field of the target, we locate the red clump. The apparent clump centroid is $(V-I, D)_{\text{clump}} = (2.215, 15.59)$. According to Bensby et al. (2013) and Nataf et al. (2013), the intrinsic color and magnitude of the red clump in the event direction are (1.06, 14.36). Using the offset between the observed and actual clump centroid as a measure of source extinction and reddening (Yoo et al. 2004), we determine the intrinsic source color and brightness to be $(V-I, D)_{0,\text{source}} = (0.808, 14.98)$. This is at the blue edge of the giant clump, which is sparsely populated. From Bessell & Brett (1988)'s color table for giants, we infer the source to be a G0 giant.

We interpolate the color tables in Bessell & Brett (1988) to arrive at $(V-K, K)_{\text{source}} = (1.78 \pm 0.04, 14.00 \pm 0.06)$. Using the relationship between stellar angular size, ($V-K$) color, and

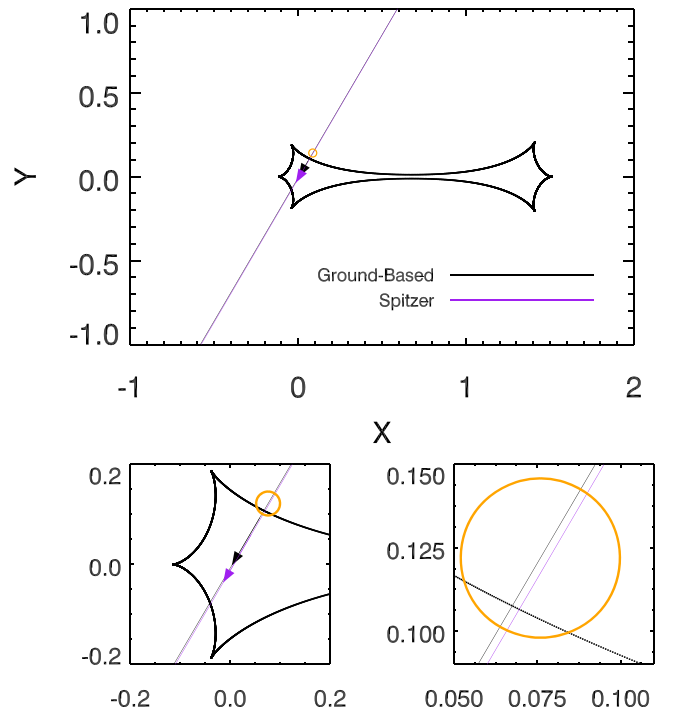


Figure 3. The $u_0 > 0$ caustic structure of the binary microlensing event OB140962. This is a resonant caustic crossing event. The source size is indicated by the orange circle. Lower panels show zoom-ins of the ground-based (black) and space-based (purple) source trajectories, with minuscule separation between them. Arrow tips coincide with t_0 for the ground-based light curve.

K magnitude given by Adams et al. (2018), we find the source angular radius $\theta_* = 3.4 \pm 0.2 \mu\text{as}$.

The source star's brightness profile, which is important for modeling the caustic crossings, is parameterized by its limb-darkening properties. Claret & Bloemen (2011) give linear limb-darkening coefficients (u) for stars with a variety of effective temperatures, surface gravities, metallicities, and microturbulences. Assuming solar metallicity, we determine T_{eff} to be 5400 ± 100 K using its relation with $V-I$ color from Casagrande et al. (2010). We adopt $\log(g) = 3$ and microturbulence ~ 2 km s $^{-1}$. The corresponding $\Gamma = (2u/(3-u))$ is 0.41 in the I band and 0.14 in the *Spitzer* L band. These Γ values are in turn used in the final fits of the light curve parameters, as described in Section 3.3.

Table 3

Measured Physical Properties of Binary Lens System OGLE-2014-BLG-0962

Quantity	Value from Best-fit Solution	
	$u_0 > 0$	$u_0 < 0$
π_E	0.049 ± 0.001	0.048 ± 0.001
θ_E (mas)	0.144 ± 0.008	0.144 ± 0.008
μ_{rel} (mas yr $^{-1}$)	8.119 ± 0.001	8.132 ± 0.001
M_{tot} (M_{\odot})	0.365 ± 0.020	0.366 ± 0.020
M_{prim} (M_{\odot})	0.204 ± 0.011	0.205 ± 0.011
M_{sec} (M_{\odot})	0.160 ± 0.009	0.161 ± 0.009
D_S (kpc)	7.863 ± 0.000	7.863 ± 0.000
D_L (kpc)	7.453 ± 0.021	7.455 ± 0.021
a_{proj} (au)	2.040 ± 0.107	2.036 ± 0.107
$D_{8.3}$ (kpc)	7.845 ± 0.021	7.847 ± 0.021
D_{LS}	0.410 ± 0.021	0.407 ± 0.021

4.2. Physical Parameters of the Lens

From the equations listed in Section 3.1, the physical properties of the system are straightforwardly determined. We display the results in Table 3. The uncertainties are derived from direct propagation. We calculate D_L , a_{proj} , and D_{LS} , assuming zero uncertainty in D_S . These final calculated properties are broadly compatible with the estimates from the earlier heuristic arguments.

Since the exact source distance is unknown, we list both $D_{8.3}$ (Calchi Novati et al. 2015a; see also Section 5.4) and D_L relative to the mean bar clump distance at the event’s Galactic coordinates, which is $D_S = 7.86$ kpc (Nataf et al. 2013). Regardless of the precise location of the source, this M+M-dwarf binary is the most distant lensing system discovered with *Spitzer*.

5. The *Spitzer* Microlens Sample: A Test Bed for Bayesian Analysis

OB140962 represents another addition to the growing sample of well-characterized microlensing systems from the *Spitzer* satellite parallax campaign. The *Spitzer* sample provides an excellent opportunity to test the accuracy of typical Bayesian priors used in microlensing for about a dozen systems (Table 5). This gives an observational test of the galactic models and provides insight into the efficacy of Bayesian estimates of the physical properties of microlenses.

The *Spitzer* set of objects have directly measured M_L and D_L , in contrast to most microlensing discoveries to date, whose physical properties are indeterminate because of the lack of constraint on π_E . For the caustic-crossing microlensing events for which only t_E and θ_E are measured, the standard way to proceed is to perform a Bayesian analysis to infer probabilistic distributions for these parameters. This involves evaluating the likelihood of particular lens–source configurations using a Galactic model prior conditioned upon the measured t_E and θ_E (taken together, they also encode the magnitude of the lens–source relative proper motion; see Equation (3)). The resulting posteriors are often broad, with CIs spanning about a half-dex in mass and 2–3 kpc in distance. In Section 5.1, we describe the ingredients that go into such an analysis.

It is important to have confidence in the conclusions from the Bayesian analysis, since this will remain the chief channel for deriving lens system properties in the absence of expensive simultaneous satellite observations (or *WFIRST*). Bayesian

analysis based on Galactic priors will continue to affect our understanding of both individual systems and ensemble statistics (e.g., Calchi Novati et al. 2015a; Penny et al. 2016). Specifically, for applications in statistical population studies, it is crucial to verify that such a method does not yield systematically biased estimates of physical parameters. Moreover, a uniform interpretation of the properties of lenses characterized with a Bayesian analysis requires knowing if different Galactic models yield comparable results.

We begin by describing the Bayesian formalism and Galactic model priors in Section 5.1. In Section 5.2, we compare the Bayesian results from each prior model tested with the measured properties for OB140962. Section 5.3 discusses the case of OB161195, a lens that has been characterized separately with *Spitzer* parallax (Shvartzvald et al. 2017) and with Bayesian analysis alone (Bond et al. 2017). Then, in Sections 5.4 and 5.5, we extend this test to the subset of *Spitzer* microlenses published to date with similarly secure characterizations.

5.1. Bayesian Formalism

The Bayesian analysis framework is based on a Galactic model prior, whose ingredients are mass functions (MF) and both velocity distributions (VD) and density profiles (DP) of the bulge and disk of the Milky Way, in the direction of the event. Each draw of a lens–source pair has a corresponding θ_E and μ_{rel} (which is interchangeable with t_E). For binary lenses, we make the following modification to the original Bayesian formalism, whose MF assumes single stars and does not account for binaries. We draw the mass of the primary component, M_{prim} , from an appropriate MF. Then we calculate M_{tot} and θ_E from $M_{\text{tot}} = M_{\text{prim}} (1 + q)$. One underlying assumption is that the binary parameters of the event (s , q) do not depend on the mass and distance of the lens. The likelihood function is constrained by the observed t_E and θ_E of the event.

Our baseline Galactic model draws from the single-star MF reported by Chabrier (2003) and derives the VD and DP from Han & Gould (1995a, 2003, hereafter collectively denoted HG). Specifically, the disk DP follows the exponential functional form of Bahcall (1986), with scale heights and thin/thick disk density normalization constants from Jurić et al. (2008). The bulge DP parameters are based on the barred model (“G2”) from Dwek et al. (1995), scaled to the stellar mass density given in Batista et al. (2011). This is described in detail in Jung et al. (2018).

We choose to test two VDs and DPs: the baseline model (HG) and that used by Zhu et al. (2017, hereafter Zhu17). The Zhu17 bulge DP and its normalization are based on Robin et al. (2003), which is more compact and has a higher stellar density contrast relative to its disk (Han & Gould 1995a) than that for our baseline model. In addition, the bulge velocity dispersions are also markedly larger for the Zhu17 VD ($\sigma_{y,z,B} = 120$ km s $^{-1}$) than for HG ($\sigma_{y,B} = 82.5$ km s $^{-1}$, $\sigma_{z,B} = 66.3$ km s $^{-1}$). Table 4 shows the four model combinations investigated in this work. We note that the Chabrier and Sumi (Sumi et al. 2011) MFs are very similar, and it has been previously demonstrated that the choice of MF makes little difference in inferring lens parameters, at least for single lenses (e.g., Zhu et al. 2017). Therefore, we use the Chabrier MF for all cases tested, excluding stellar remnants for events involving planetary lenses.

Table 4
Galactic Model Priors

Model	VD	DP
1 (Baseline HG)	HG	HG
2 (Zhu17 DP)	HG	Zhu17
3 (Zhu17 VD)	Zhu17	HG
4 (Zhu17)	Zhu17	Zhu17

Note.

HG refers to Han & Gould (1995a, 2003) and references therein, with DP scaling from Batista et al. (2011; see also Jung et al. 2018). Zhu17 refers to Zhu et al. (2017) and references therein. All models use the Chabrier single-star MF (Chabrier 2003), with stellar remnants excluded for putative planet hosts ($q < 0.05$).

5.2. OB140962

We input our best-fit θ_E and t_E values from the $u_0 > 0$ solution into a Bayesian analysis with our baseline Galactic model. Figure 4 displays the posterior distributions for M_{prim} and D_{LS} . For lenses in the bulge, D_{LS} is a more robust metric than D_L , since it is comparatively less sensitive to the uncertainty in the source distance. The directly measured quantities are overplotted. Bayesian analysis indicates that the lens’s primary has $\log(M_{\text{prim}}/M_{\odot}) = -1.17^{+0.43}_{-0.35}$ or $M_{\text{prim}} = 0.07^{+0.11}_{-0.04} M_{\odot}$. The true value of $M_{\text{prim}} \sim 0.20$ is just outside the 68% CI. In this case, the difference between the Bayesian value and the true value means the difference between a BD binary detection and a run-of-the-mill M+M binary. Similarly, taking D_S to be the clump distance in the direction of this event (Nataf et al. 2013), we find that the parallax-derived value of $D_{LS} = 0.41$ kpc is just outside the 68% CI of the Bayesian prediction for the lens–source distance $D_{LS} = 1.31^{+1.22}_{-0.77}$ kpc. We repeat this analysis for Galactic models 2–4. In case 2, $M_{\text{prim}} = 0.08^{+0.11}_{-0.04} M_{\odot}$ and $D_{LS} = 1.11^{+0.83}_{-0.61}$ kpc. Case 3 returns $M_{\text{prim}} = 0.08^{+0.13}_{-0.04} M_{\odot}$ and $D_{LS} = 1.28^{+1.16}_{-0.75}$ kpc. In case 4, $M_{\text{prim}} = 0.11^{+0.16}_{-0.05} M_{\odot}$ and $D_{LS} = 0.92^{+0.78}_{-0.51}$ kpc.

The very small π_E measured by *Spitzer* places the true lens very close to the source star. In all cases, the mass and distance ($D_L = D_S - D_{LS}$) are underpredicted. It is clear that *Spitzer* has provided important added value for accurately determining the mass and distance to this microlens.

5.3. OB161195

Another noteworthy lens with *Spitzer* parallax is OB161195 (Shvartzvald et al. 2017), which has been independently analyzed by Bond et al. (2017) using Bayesian analysis alone. The physical properties derived from parallax are $M_L = 0.078^{+0.016}_{-0.012} M_{\odot}$ and $D_L = 3.91^{+0.42}_{-0.46}$ kpc (Shvartzvald et al. 2017). This is between the 68% and 95% CIs of Bond et al. (2017), which yielded $M_L = 0.37^{+0.38}_{-0.21}$ and $D_L = 7.20^{+0.85}_{-1.02}$.

Our Bayesian posteriors for this lens system according to the baseline model are $M_L = 0.20^{+0.25}_{-0.11} M_{\odot}$ and $D_L = 6.41^{+1.20}_{-1.49}$ kpc, which differ from those of Bond et al. (2017). The main source of the discrepancy arises from differences in the Galactic models assumed. Bond et al. (2017) uses a bulge VD with $\sigma_y = 103.8$ km s $^{-1}$, $\sigma_z = 96.4$ km s $^{-1}$, but also includes a bulge (solid body) rotation of 50 km s $^{-1}$ kpc $^{-1}$. In addition, the VDs are truncated at 600 km s $^{-1}$ in the bulge and 550 km s $^{-1}$ in the other components. For their DP, they also

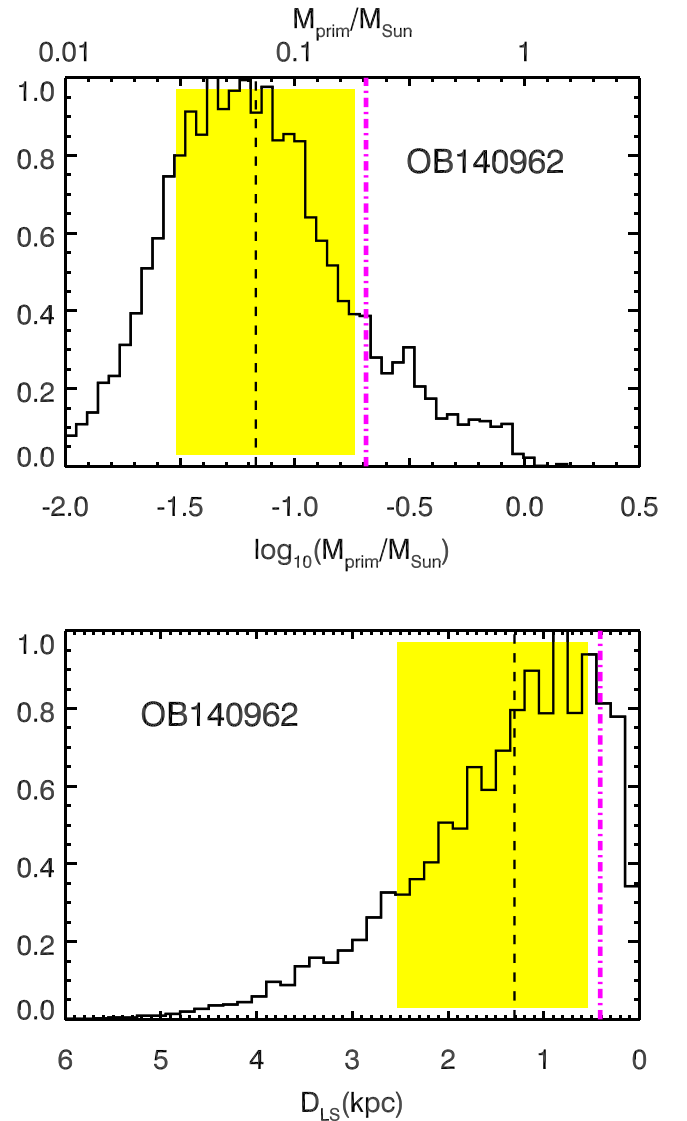


Figure 4. Posteriors of lens physical properties (M_{prim} and D_{LS}) for OB140962 based on Bayesian analysis with the baseline Galactic model. The Bayesian median is demarcated by the black dashed verticals, while the yellow shaded boxes outline the 68% CIs about the median. Overplotted in the magenta dashed-dotted lines are the values measured directly from *Spitzer* parallax. Whereas the Bayesian analysis argues for a brown dwarf binary, the *Spitzer* measurement clearly attributes the event to a mid-M+M-dwarf binary lens very close to the Galactic center. Only $\sim 13\%$ ($\sim 12\%$) of the Bayesian posterior lies above (below) the true M_L (D_{LS}).

include thick disk and spheroid components. They use the Sumi MF, but this should not have a significant effect because of the similarity to the Chabrier MF. Finally, we note that our analysis is based on the t_E and θ_E given in Shvartzvald et al. (2017), whereas Bond et al. (2017) measure a slightly larger t_E and smaller θ_E . This does have a small effect on the results, but the biggest effects are due to differences in the Galactic models.

The case of OB161195 indicates that the assumption of Galactic models can affect the conclusions. At the same time, it is worth noting that OB161195 is kinematically peculiar: despite its disk-like distance, its motion is not in the direction of the disk’s rotation (Shvartzvald et al. 2017). For a Bayesian analysis based on θ_E and t_E , the direction of the motion would

be unknown. Therefore, with this knowledge, we recognize that a Bayesian analysis may not accurately reflect the properties of OB161195.

5.4. Assembling the Spitzer Microlensing Sample

Bayesian analysis is expected to give a statistical representation of the truth. As such, it is not in itself surprising that individual outliers like OB140962 and OB161195 exist. The growing inventory of objects with *Spitzer* satellite parallaxes allows us to investigate whether there are systematic problems with the Bayesian framework for a larger sample, specifically the consistency with and dependence on Galactic models.

Here we describe a set of 13 published *Spitzer* events (including OB140962) with unique measurements of both π_E and θ_E , for which we test the Bayesian analyses. Their relevant measured properties are given in Tables 5 and 6, where the tabulated lens masses, distances, and their uncertainties are computed from the θ_E and π_E values given in the literature using Equation (4). Among their ranks are both two-body lenses and single lenses with securely modeled finite-source effects. For events with degeneracies for which the authors advocate strongly for one particular solution for θ_E and π_E based either on χ^2 fitness or on physical grounds (OB140289: Udalski et al. 2018; OB141050: Zhu et al. 2015; OB161045: Shin et al. 2018; OB161190: Ryu et al. 2018), we retain the favored solutions only. Events with degeneracies yielding physical properties consistent within 1σ are assigned physical properties corresponding to the solution with the lowest χ^2 for this comparison (OB140124: Udalski et al. 2015b; Beaulieu et al. 2018; OB141050: Zhu et al. 2015; OB150479: Han et al. 2016; OB161195: Shvartzvald et al. 2017). Note that, although membership in our sample requires selection for *Spitzer* follow-up, it is not necessarily true that both θ_E and π_E were immediately constrained by the *Spitzer* plus ground observations. For OB140124, θ_E is not well measured, due to the absence of the finite source effect. Therefore, we assign to it physical parameters determined by follow-up AO imaging (Beaulieu et al. 2018). In the case of OB140289, *Spitzer* could not constrain π_E because it happened to observe a featureless region of the light curve. Fortunately, this event is sufficiently long that annual parallax could be accurately and precisely determined.

We exclude from our Bayesian sample the events with severe degeneracies, that is, those with multiple solutions for which the physical properties M_L and D_L are incompatible within their nominal uncertainties (OB150196: Han et al. 2017; OB151482: Chung et al. 2017; OB170329: Han et al. 2018). It would be difficult to interpret a comparison between the Bayesian results and quantities that are ill defined. We also exclude OB151285 (Shvartzvald et al. 2015) and OB161266 (Albrow et al. 2018) from this exercise because the Bayesian priors for the MF of planetary-mass objects and stellar remnants are not well understood.

For the purpose of this comparison, we use

$$D_{8.3} = \frac{\text{kpc}}{\pi_{\text{rel}}/\text{mas} + 1/8.3} \quad (7)$$

as our distance metric (Calchi Novati et al. 2015a). This metric is independent of uncertainties in the source distance and is

well defined for lenses in both the disk and the bulge. The first point is significant, because the literature does not homogeneously report the source distance assumed in the D_L calculation, and the Bayesian analysis draws sources from a range of distances in the bulge.

5.5. Galactic Model Tests

As for OB140962 (Section 5.2), we now compute Bayesian posteriors for lens mass and distance for all 13 objects using galactic models given in Table 4. We treat binaries as described in Section 5.1. For planetary events (defined for this purpose to be $q < 0.05$), we exclude stellar remnants from the Galactic models. The results are summarized in Table 6.

Figure 5 shows the comparison between the output from the baseline Galactic model and the values calculated from parallax. For the majority of the cases, the Bayesian posteriors are consistent with the true measured values. OB140962 is one of the objects for which the true values are in tension with the Bayesian predictions (see Section 5.2). For both mass and distance, the true values lie above the 84th percentile of the Bayesian posteriors. However, if the posteriors are true representations of the data, occasional outliers are expected. In fact, this particular situation should occur for 16% of the instances.

To test the overall accuracy of the baseline model, we evaluate the fraction of posterior lying above the true values of M_L and $D_{8.3}$ derived from parallax for each object in this ensemble. If these Bayesian posteriors represent the true values fairly for this ensemble, we should expect this cumulative distribution function (CDF) to follow the identity function (e.g., 10% of the time the true value falls below 10% of the posterior). In Figure 6, the black solid line shows the cumulative distribution of the fraction of posterior lying above the parallax value for M_L and $D_{8.3}$. One-sample Kolmogorov–Smirnov (KS) tests show that the distributions for the two parameters are consistently distributed around the one-to-one line. This indicates that, on average, Bayesian analysis with our baseline Galactic model is a reasonable reflection of the data. Of course, a direct measurement (e.g., with parallax or AO observations) is still necessary to correctly identify the nature of any given individual object.

Agreement with the other three Galactic models tested are comparably good. The last row of Table 6 shows the p values from the one-sample KS test for the Bayesian posteriors of the two physical parameters for each model, with their CDFs also plotted in Figure 6. The KS test shows that all models are overall consistent with the *Spitzer* sample. However, there are some systematic effects between model predictions. For objects perceived to be near the Galactic bulge (Bayes $D_{8.3} \gtrsim 6$ kpc), models using the Zhu17 DPs tend to predict greater lens mass and distance than those from the HG DPs (see Table 6). This can be attributed to the relatively higher stellar density and compactness of the bulge component in the Zhu17 DP compared to in HG. Therefore, the DP of Zhu17 has a greater tendency to “pull” a lens that already appears to be close to the bulge even closer in toward the Galactic center, which increases the inferred distance. To conserve the observed θ_E , the inferred mass is increased as well (see Equation (2)). While this discrepancy is much smaller than the typical uncertainties, it is a systematic effect

Table 5
Spitzer Bayesian and Binary Sample Properties

Object Abbrev	Deg Solution	l	b	θ_E	t_E (days)	π_E	$\mu_{\text{hel},l}$ (mas yr $^{-1}$)	$\mu_{\text{hel},b}$ (mas yr $^{-1}$)	$D_{8.3}$ (kpc)	$M_{L,\text{tot}}$ (M_\odot)	q^a	Bayes ^b	Bin ^c	References ^d
OB140124	++	2.34	-2.92	1.030 ± 0.060	150.80 ± 2.80	0.146	1.60	-3.02	3.7	0.90	6.9e-04	Y	Y	(1), (15)
OB140289	++	0.80	-1.62	1.170 ± 0.090	144.43 ± 0.24	0.152	1.40	1.91	3.4	0.94	8.1e-01	Y	Y	(2)
OB140962		2.66	-2.54	0.144 ± 0.008	6.45 ± 0.03	0.049	5.12	-6.36	7.8	0.36	7.9e-01	Y	Y	(3)
OB141050	++	5.09	3.23	1.340 ± 0.160	73.30 ± 4.20	0.120	1.48	-7.38	3.6	1.37	3.9e-01	Y	Y	(4)
OB150020		-2.24	-3.16	1.329 ± 0.049	63.55 ± 0.06	0.223	-5.88	-4.67	2.4	0.73	2.1e-01	Y	Y	(5)
OB150479	-	-5.82	-3.08	1.870 ± 0.430	86.30 ± 0.50	0.125	-6.09	2.86	2.8	1.83	8.1e-01	Y	Y	(6)
OB150763	-+	-1.85	2.25	0.288 ± 0.020	32.78 ± 0.25	0.071	2.94	1.32	7.1	0.50	...	Y	N	(7)
OB150966	-close	0.96	-1.82	0.760 ± 0.070	57.80 ± 0.40	0.241	-2.57	2.70	3.3	0.39	1.7e-04	Y	Y	(8)
OB151268		7.34	1.42	0.127 ± 0.009	17.50 ± 0.70	0.347	2.68	-0.97	6.1	0.05	...	Y	N	(7)
OB151319	-- wide	-1.71	-4.05	0.660 ± 0.070	98.80 ± 4.80	0.124	-0.02	2.00	4.9	0.65	9.5e-02	N	Y	(9)
OB160168		-1.84	-2.42	1.410 ± 0.120	93.67 ± 1.17	0.363	6.12	1.13	1.6	0.48	7.7e-01	Y	Y	(10)
OB161045	--	-5.75	-1.39	0.245 ± 0.015	11.98 ± 0.08	0.355	5.86	-5.41	4.8	0.08	...	Y	N	(11)
OB161190		2.62	-1.84	0.490 ± 0.040	93.53 ± 0.89	0.067	1.77	0.67	6.5	0.90	1.5e-02	Y	Y	(12)
OB161195	-- close	-0.00	-2.48	0.286 ± 0.050	9.96 ± 0.11	0.473	0.29	9.76	3.9	0.07	5.5e-05	Y	Y	(13)
OB161266	A-	-0.04	-1.50	0.227 ± 0.011	8.65 ± 0.08	0.971	9.92	-0.17	2.9	0.03	7.6e-01	N	Y	(14)

Notes.

^a ... denotes single lenses for which the notion of q is not applicable.

^b Whether or not the object is included in the Bayesian analysis.

^c Whether or not the object is included in the binarity analysis.

^d **References.** (1) Udalski et al. (2015b), (2) Udalski et al. (2018), (3) this work, (4) Zhu et al. (2015), (5) Wang et al. (2017), (6) Han et al. (2016), (7) Zhu et al. (2016), (8) Street et al. (2016), (9) Shvartzvald et al. (2016a), (10) Shin et al. (2017), (11) Shin et al. (2018), (12) Ryu et al. (2018), (13) Shvartzvald et al. (2017), (14) Albrow et al. (2018), (15) Beaulieu et al. (2018).

Table 6
Lens Properties: Measured vs. Bayesian

Object Abbrev	Measured		Bayesian Model 1		Bayesian Model 2		Bayesian Model 3		Bayesian Model 4	
	$M_{\text{prim}} (M_{\odot})$	$D_{8.3}$ (kpc)	$M_{\text{prim}} (M_{\odot})$	$D_{8.3}$ (kpc)	$M_{\text{prim}} (M_{\odot})$	$D_{8.3}$ (kpc)	$M_{\text{prim}} (M_{\odot})$	$D_{8.3}$ (kpc)	$M_{\text{prim}} (M_{\odot})$	$D_{8.3}$ (kpc)
OB140124 ^a	0.90 ± 0.05	3.70 ± 0.20	$0.78^{+0.41}_{-0.36}$	$3.45^{+0.90}_{-1.13}$	$0.72^{+0.41}_{-0.33}$	$3.29^{+0.92}_{-1.11}$	$0.82^{+0.42}_{-0.38}$	$3.53^{+0.90}_{-1.17}$	$0.75^{+0.40}_{-0.35}$	$3.36^{+0.96}_{-1.13}$
OB140289 ^b	0.52 ± 0.04	3.35 ± 0.16	$0.75^{+0.38}_{-0.32}$	$4.06^{+0.95}_{-1.12}$	$0.69^{+0.33}_{-0.31}$	$3.82^{+0.90}_{-1.07}$	$0.78^{+0.55}_{-0.32}$	$4.19^{+1.11}_{-1.14}$	$0.72^{+0.45}_{-0.34}$	$3.94^{+1.14}_{-1.19}$
OB140962	0.20 ± 0.01	7.85 ± 0.02	$0.07^{+0.11}_{-0.04}$	$7.11^{+0.74}_{-1.10}$	$0.08^{+0.11}_{-0.04}$	$7.32^{+0.57}_{-0.80}$	$0.08^{+0.13}_{-0.04}$	$7.21^{+0.69}_{-0.95}$	$0.11^{+0.16}_{-0.05}$	$7.50^{+0.50}_{-0.68}$
OB141050	0.99 ± 0.28	3.55 ± 0.57	$0.82^{+0.54}_{-0.33}$	$3.36^{+1.09}_{-1.04}$	$0.80^{+0.56}_{-0.33}$	$3.27^{+1.13}_{-1.04}$	$0.82^{+0.54}_{-0.33}$	$3.28^{+1.12}_{-1.01}$	$0.80^{+0.58}_{-0.33}$	$3.20^{+1.20}_{-1.01}$
OB150020	0.60 ± 0.03	2.40 ± 0.07	$0.88^{+0.55}_{-0.38}$	$3.11^{+1.08}_{-1.02}$	$0.86^{+0.56}_{-0.38}$	$3.06^{+1.11}_{-1.05}$	$0.89^{+0.51}_{-0.34}$	$3.09^{+0.91}_{-0.88}$	$0.86^{+0.52}_{-0.32}$	$3.03^{+0.96}_{-0.87}$
OB150479	1.01 ± 0.25	2.82 ± 0.45	$0.82^{+0.55}_{-0.33}$	$3.49^{+1.41}_{-1.35}$	$0.79^{+0.54}_{-0.33}$	$3.41^{+1.41}_{-1.35}$	$0.86^{+0.57}_{-0.35}$	$3.34^{+1.43}_{-1.24}$	$0.84^{+0.58}_{-0.35}$	$3.26^{+1.44}_{-1.23}$
OB150763	0.50 ± 0.03	7.09 ± 0.07	$0.42^{+0.31}_{-0.21}$	$6.90^{+0.56}_{-0.99}$	$0.57^{+0.26}_{-0.23}$	$7.24^{+0.33}_{-0.56}$	$0.42^{+0.30}_{-0.22}$	$6.90^{+0.56}_{-1.08}$	$0.57^{+0.27}_{-0.23}$	$7.24^{+0.34}_{-0.57}$
OB150966	0.39 ± 0.04	3.30 ± 0.19	$0.76^{+0.41}_{-0.37}$	$4.70^{+0.92}_{-1.39}$	$0.69^{+0.44}_{-0.35}$	$4.46^{+1.09}_{-1.40}$	$0.73^{+0.40}_{-0.36}$	$4.57^{+0.98}_{-1.38}$	$0.65^{+0.44}_{-0.33}$	$4.31^{+1.13}_{-1.38}$
OB151268	0.05 ± 0.01	6.08 ± 0.35	$0.11^{+0.16}_{-0.06}$	$7.19^{+0.67}_{-0.93}$	$0.14^{+0.20}_{-0.07}$	$7.47^{+0.50}_{-0.63}$	$0.11^{+0.16}_{-0.06}$	$7.17^{+0.68}_{-1.00}$	$0.14^{+0.20}_{-0.07}$	$7.47^{+0.48}_{-0.67}$
OB160168	0.27 ± 0.03	1.58 ± 0.14	$0.87^{+0.53}_{-0.34}$	$3.65^{+1.07}_{-1.01}$	$0.85^{+0.56}_{-0.34}$	$3.58^{+1.13}_{-1.02}$	$0.85^{+0.54}_{-0.34}$	$3.58^{+1.03}_{-1.02}$	$0.84^{+0.60}_{-0.35}$	$3.54^{+1.19}_{-1.05}$
OB161045	0.08 ± 0.01	4.82 ± 0.15	$0.24^{+0.33}_{-0.13}$	$6.67^{+0.87}_{-1.34}$	$0.30^{+0.32}_{-0.18}$	$6.94^{+0.67}_{-1.44}$	$0.28^{+0.32}_{-0.16}$	$6.85^{+0.72}_{-1.25}$	$0.44^{+0.28}_{-0.25}$	$7.30^{+0.39}_{-0.99}$
OB161190	0.88 ± 0.08	6.52 ± 0.13	$0.67^{+0.27}_{-0.33}$	$6.12^{+0.51}_{-1.32}$	$0.81^{+0.18}_{-0.33}$	$6.44^{+0.33}_{-0.90}$	$0.60^{+0.32}_{-0.32}$	$5.92^{+0.68}_{-1.50}$	$0.74^{+0.23}_{-0.44}$	$6.31^{+0.43}_{-1.68}$
OB161195	0.07 ± 0.01	3.91 ± 0.38	$0.20^{+0.25}_{-0.11}$	$6.41^{+0.95}_{-1.33}$	$0.26^{+0.26}_{-0.14}$	$6.91^{+0.66}_{-1.23}$	$0.27^{+0.27}_{-0.14}$	$6.58^{+0.78}_{-1.13}$	$0.38^{+0.29}_{-0.19}$	$7.05^{+0.51}_{-0.80}$
<i>p</i> -Value	0.42	0.17	0.53	0.34	0.24	0.17	0.29	0.30

Notes. Measured values are calculated from θ_E and π_E measured based on *Spitzer* parallax as reported in the literature, except where noted otherwise; Bayesian values shown are median and symmetric 68% CIs.

^a Measured values come from the *Spitzer* parallax plus AO imaging (Beaulieu et al. 2018).

^b Measured values come from the finite source effect plus precise ground-based modeling of the annual parallax (Udalski et al. 2018).

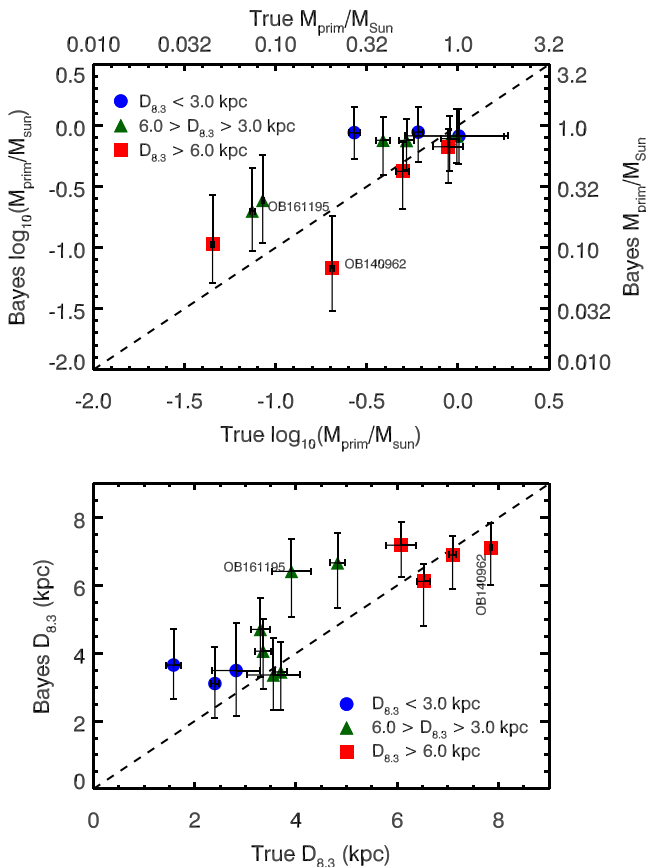


Figure 5. Comparison between physical lens system properties M_L and $D_{8.3}$ from Bayesian analysis with the baseline model and those derived from the parallax measurements, for *Spitzer* lenses with unique, unambiguous solutions. For the most part, there is good agreement.

that should be acknowledged when combining lens properties inferred from Bayesian analyses with different Galactic model priors.

6. The Galactic Distribution of *Spitzer* Binary Lenses

Ultimately, the *Spitzer* planetary systems will be analyzed to determine whether or not planet occurrence varies across the Galaxy. One way to do this is to compare the distance distribution of planetary lenses to that of the *Spitzer* single-lens sample (Calchi Novati et al. 2015a; Zhu et al. 2017). Note that Penny et al. (2016) undertook a related study, in which they compared ground-based planet discoveries with a simulated host population.

While the *Spitzer* planet sample is not yet large enough to perform this test, the number of *Spitzer* two-body lenses (both planets and binaries) is now comparable to the total number of planets expected for the full *Spitzer* sample. Thus, we can use the *Spitzer* binaries to illustrate the methodology for comparing distance distributions. To date, 12 binary lenses from *Spitzer* have published parameters with unambiguous or strongly preferred solutions, and therefore $D_{8.3}$ (Table 5). In this count, we excluded OB151212 (Bozza et al. 2016) because only three of eight degenerate solutions have constrained $D_{8.3}$. We also discarded OB150196 (Han et al. 2017) and OB170329 (Han et al. 2018) because they have severe discrete degeneracies.

Figure 7 shows the empirical binary cumulative distance distribution for these 12 events. Note that, although OB151319 (Shvartzvald et al. 2016a) was excluded from the Bayesian exercise because its eight degenerate solutions span primary masses of 0.53–0.67 M_{\odot} and fail our criteria for mass consistency, it is included here as one entry (with $D_{8.3}$ of the solution with the best χ^2) because the $D_{8.3}$ values for all degenerate solutions are actually all consistent with each other. The substellar binary candidate OB161266 (Albrow et al. 2018), previously excluded from the Bayesian sample (see Section 5.4), also enters into this analysis using $D_{8.3}$ from the “A” solution.

Overplotted on Figure 7 is the cumulative distance distribution of *Spitzer* single-lens detections from Zhu et al. (2017, the “Standard” distribution from Figure 12). An excess of binary lenses is visually apparent at intermediate distances

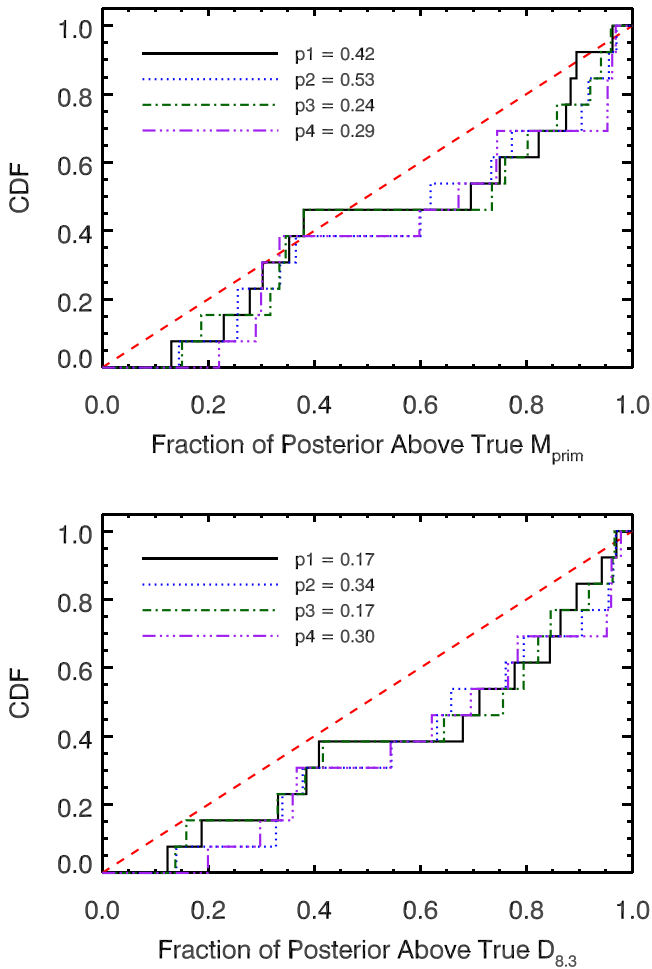


Figure 6. Empirical cumulative distribution function of Bayesian posterior fractions above the lens system’s physical properties (M_L and $D_{8.3}$) derived from parallax, for *Spitzer* lenses with unique, unambiguous solutions. The distributions are consistent with one-to-one for all of the models tested, suggesting that Bayesian posteriors produced from them are a fair representation of the underlying true parameters.

($D_{8.3} = 3\text{--}5$ kpc). To quantify this visual discrepancy, we perform a one-sample KS test for the empirical CDF. Formally, at a p value of 0.025, the null hypothesis that the binary and single lens samples are drawn from the same distribution can be rejected at 2σ significance.

Investigating the source of this intermediate-distance excess relative to the bulge is outside the scope of this paper, because any physical conclusions would first require disentangling the contribution from selection effects. While the selection effects should be the same for planets compared to single lenses, this is not necessarily true for binaries (see Yee et al. 2015a). For example, some binaries are discovered serendipitously as part of the single-lens sample selected for *Spitzer* follow-up, whereas others are deliberately observed by *Spitzer* after their binary anomalies are already detected from the ground. One indication of possible selection bias between single and two-body *Spitzer* lenses is displayed in the bottom panel of Figure 7, which shows a 3σ discrepancy (from a two-sample KS test) between the t_E distributions of single and binary lenses. The figure gives the t_E directly from the model (which is relative to the total mass of the system) and the t_E relative to the primary alone. The latter is the most relevant comparison for single lenses because it shows what would have been observed

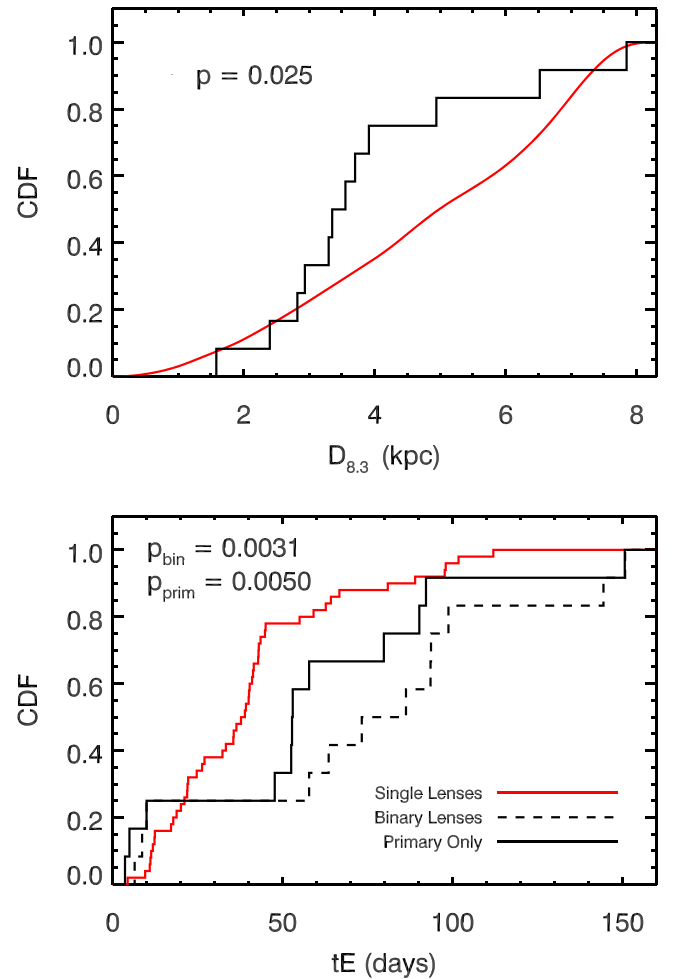


Figure 7. Top panel: the empirical cumulative distance distribution function of *Spitzer* binary lenses (black), overplotted on the *Spitzer* single-lens detections from 2015 (red). The binary ensemble has only a 2.5% probability of being drawn from the single-lens distribution. Bottom panel: the cumulative distribution of t_E for single lenses (red) and binary lenses (black), with the distribution of t_E calculated from the primary component of the binary lens denoted by the black solid line. Based on a two-sample KS test, the single and binary lens distributions are discrepant at the 3σ level.

in the absence of a companion. The discrepancy in the t_E distribution likely contributes to the excess at intermediate distances, but even the origin of the t_E discrepancy is unknown (possibly related to selection effects). Regardless of the physical explanation for the excess at 3–5 kpc, the above analysis shows that this method can measure significant differences in the distance distribution of a population with only 12 objects relative to the single-lens population.

7. Summary

Measurements of the Einstein radius (θ_E) and the microlens parallax (π_E) make a powerful combination for deducing the physical properties of lensing systems, such as mass, distance, and kinematics. This information is readily available for events involving binary lenses with satellite observations. However, for many ground-based microlensing discoveries, it is not possible to obtain both quantities for an unambiguous solution. In these cases, a Bayesian analysis, based on a Galactic model, is used to give a probabilistic estimate of the physical parameters. The interpretation of many individual systems

and ensemble statistics depends on the accuracy of the Bayesian analysis and the Galactic models that go into it, which we systematically test in this work.

We first present the discovery and characterization of OGLE-2014-BLG-0962 using high-quality ground-based survey and *Spitzer* data. The densely covered light curves allow us to constrain θ_E and π_E very well, leading to a unique interpretation of this object being a textbook mid-M-M stellar binary deeply embedded in the Galactic bulge. However, the angular Einstein radius (0.14 mas) is on the small side. Thus, if we were to infer the physical properties of this system without using the parallax information—that is, using a standard Bayesian analysis based on a Galactic model prior—we would infer a much lower lens mass.

To investigate whether the Bayesian framework is on average reliable and the consistency of different Galactic model priors, we assemble a sample of 13 well-understood *Spitzer* systems and perform Bayesian analyses on each of them using their t_E and θ_E as inputs. We test four representative sets of Galactic models. Comparing the Bayesian predictions of lens mass (M_L) and lens–source distance ($D_{8.3}$) to the same physical properties calculated from π_E , we find good agreement overall for all models tested; that is, the Bayesian posteriors are on average representative of the true answers. Nevertheless, small systematic differences exist between the model predictions, and care should be taken when combining measurements based on different Galactic model priors.

We also construct a sample of *Spitzer* binaries and show the methodology for making quantitative statements about the Galactic distribution of planetary and binary lenses using detections from *Spitzer*. A comparison with that of single-lens detections from *Spitzer* shows tentative evidence that the two types of lenses are drawn from incompatible distance distributions. Specifically, binaries may be more abundant relative to single stars at the intermediate distances (i.e., 3–5 kpc) and deficient beyond ~ 6 kpc, the latter coinciding with the geographical location of the Galactic bulge. We do not investigate the reason for this discrepancy, which could be related to the difference in the t_E distributions or other selection effects. However, while understanding the exact source of this excess lies outside the scope of this work, we have demonstrated our ability to measure a significant difference between a reference spatial distribution function and that of a sample of interest with just 12 objects. Our finding bodes well for the primary mission of the *Spitzer* microlensing campaign to constrain the Galactic distribution of planets using a similarly sized sample.

The authors would like to thank John Johnson, Jason Eastman, and other members of the Exolab for providing helpful suggestions and feedback throughout the course of this work. We are grateful to Vinay Kashyap for his statistical guidance. We thank Wei Zhu for contributing the data for the *Spitzer* single-lens CDF (Figure 12 of Zhu et al. 2017) and for discussions. Y. Shan is supported in part by a Doctoral Postgraduate Scholarship from the Natural Science and Engineering Research Council (NSERC) of Canada. The OGLE project has received funding from the National Science Centre, Poland, grant MAESTRO 2014/14/A/ST9/00121 to A.U. The OGLE Team thanks Profs. M. Kubiak and G. Pietrzyński for their contribution to the OGLE photometric data set. The MOA project is supported by JSPS KAKENHI

grant Nos. JSPS24253004, JSPS26247023, JSPS23340064, JSPS15H00781, and JP16H06287. This research was supported by the I-CORE program of the Planning and Budgeting Committee and the Israel Science Foundation, grant 1829/12. D.M. and A.G. acknowledge support by the U.S.–Israel Binational Science Foundation.

ORCID iDs

Jennifer C. Yee  <https://orcid.org/0000-0001-9481-7123>
 Yossi Shvartzvald  <https://orcid.org/0000-0003-1525-5041>
 In-Gu Shin  <https://orcid.org/0000-0002-4355-9838>
 Youn-Kil Jung  <https://orcid.org/0000-0002-0314-6000>
 Sebastiano Calchi Novati  <https://orcid.org/0000-0002-7669-1069>
 Sean Carey  <https://orcid.org/0000-0002-0221-6871>
 B. Scott Gaudi  <https://orcid.org/0000-0003-0395-9869>
 Richard W. Pogge  <https://orcid.org/0000-0003-1435-3053>
 Radosław Poleski  <https://orcid.org/0000-0002-9245-6368>
 Jan Skowron  <https://orcid.org/0000-0002-2335-1730>
 Szymon Kozłowski  <https://orcid.org/0000-0003-4084-880X>
 Przemysław Mróz  <https://orcid.org/0000-0001-7016-1692>
 Paweł Pietrukowicz  <https://orcid.org/0000-0002-2339-5899>
 Igor Soszyński  <https://orcid.org/0000-0002-7777-0842>
 Krzysztof Ulaczyk  <https://orcid.org/0000-0001-6364-408X>
 David P. Bennett  <https://orcid.org/0000-0001-8043-8413>
 Akihiko Fukui  <https://orcid.org/0000-0002-4909-5763>
 Yoshitaka Itow  <https://orcid.org/0000-0002-8198-1968>
 Kohei Kawasaki  <https://orcid.org/0000-0003-2006-1735>
 Naoki Koshimoto  <https://orcid.org/0000-0003-2302-9562>
 Shota Miyazaki  <https://orcid.org/0000-0001-9818-1513>
 Clément Ranc  <https://orcid.org/0000-0003-2388-4534>
 Nicholas J. Rattenbury  <https://orcid.org/0000-0001-5069-319X>
 Daisuke Suzuki  <https://orcid.org/0000-0002-5843-9433>

References

- Adams, A. D., Boyajian, T. S., & von Braun, K. 2018, *MNRAS*, 473, 3608
 Alard, C., & Lupton, R. H. 1998, *ApJ*, 503, 325
 Albrow, M. D., Horne, K., Bramich, D. M., et al. 2009, *MNRAS*, 397, 2099
 Albrow, M. D., Yee, J. C., Udalski, A., et al. 2018, *ApJ*, 858, 107
 Awiphan, S., Kerins, E., & Robin, A. C. 2016, *MNRAS*, 456, 1666
 Bahcall, J. N. 1986, *ARA&A*, 24, 577
 Batista, V., Beaulieu, J.-P., Bennett, D. P., et al. 2015, *ApJ*, 808, 170
 Batista, V., Beaulieu, J.-P., Gould, A., et al. 2014, *ApJ*, 780, 54
 Batista, V., Gould, A., Dieters, S., et al. 2011, *A&A*, 529, A102
 Beaulieu, J.-P., Batista, V., Bennett, D. P., et al. 2018, *AJ*, 155, 78
 Bennett, D. P., Batista, V., Bond, I. A., et al. 2014, *ApJ*, 785, 155
 Bennett, D. P., Bhattacharya, A., Anderson, J., et al. 2015, *ApJ*, 808, 169
 Bensby, T., Yee, J. C., Feltzing, S., et al. 2013, *A&A*, 549, A147
 Bessell, M. S., & Brett, J. M. 1988, *PASP*, 100, 1134
 Bond, I. A., Abe, F., Dodd, R. J., et al. 2001, *MNRAS*, 327, 868
 Bond, I. A., Bennett, D. P., Sumi, T., et al. 2017, *MNRAS*, 469, 2434
 Bozza, V., Shvartzvald, Y., Udalski, A., et al. 2016, *ApJ*, 820, 79
 Calchi Novati, S., Gould, A., Udalski, A., et al. 2015a, *ApJ*, 804, 20
 Calchi Novati, S., Gould, A., Yee, J. C., et al. 2015b, *ApJ*, 814, 92
 Casagrande, L., Ramírez, I., Meléndez, J., Bessell, M., & Asplund, M. 2010, *A&A*, 512, A54
 Chabrier, G. 2003, *PASP*, 115, 763
 Chung, S.-J., Zhu, W., Udalski, A., et al. 2017, *ApJ*, 838, 154
 Claret, A., & Bloemen, S. 2011, *A&A*, 529, A75
 Dong, S., DePoy, D. L., Gaudi, B. S., et al. 2006, *ApJ*, 642, 842
 Dwek, E., Arendt, R. G., Hauser, M. G., et al. 1995, *ApJ*, 445, 716
 Gould, A. 1994, *ApJL*, 421, L75
 Gould, A. 2000, *ApJ*, 542, 785
 Gould, A. 2008, *ApJ*, 681, 1593
 Gould, A., Udalski, A., An, D., et al. 2006, *ApJL*, 644, L37

- Han, C., Calchi Novati, S., Udalski, A., et al. 2018, *ApJ*, 859, 82
- Han, C., & Gould, A. 1995a, *ApJ*, 447, 53
- Han, C., & Gould, A. 1995b, *ApJ*, 449, 521
- Han, C., & Gould, A. 2003, *ApJ*, 592, 172
- Han, C., Udalski, A., Gould, A., et al. 2016, *ApJ*, 828, 53
- Han, C., Udalski, A., Gould, A., et al. 2017, *ApJ*, 834, 82
- Jung, Y. K., Udalski, A., Gould, A., et al. 2018, *AJ*, 155, 219
- Jurić, M., Ivezić, Ž., Brooks, A., et al. 2008, *ApJ*, 673, 864
- Kayser, R., Refsdal, S., & Stabell, R. 1986, *A&A*, 166, 36
- Wyrzykowski, Ł., Kostrzewa-Rutkowska, Z., Skowron, J., et al. 2016, *MNRAS*, 458, 3012
- Mróz, P., Ryu, Y.-H., Skowron, J., et al. 2018, *AJ*, 155, 121
- Mróz, P., Udalski, A., Skowron, J., et al. 2017, *Natur*, 548, 183
- Nataf, D. M., Gould, A., Fouqué, P., et al. 2013, *ApJ*, 769, 88
- Pejcha, O., & Heyrovský, D. 2009, *ApJ*, 690, 1772
- Penny, M. T., Gaudi, B. S., Kerins, E., et al. 2018, arXiv:1808.02490
- Penny, M. T., Henderson, C. B., & Clanton, C. 2016, *ApJ*, 830, 150
- Penny, M. T., Kerins, E., Rattenbury, N., et al. 2013, *MNRAS*, 434, 2
- Refsdal, S. 1966, *MNRAS*, 134, 315
- Robin, A. C., Reylé, C., Derrière, S., & Picaud, S. 2003, *A&A*, 409, 523
- Ryu, Y.-H., Yee, J. C., Udalski, A., et al. 2018, *AJ*, 155, 40
- Schneider, P., & Weiss, A. 1986, *A&A*, 164, 237
- Shin, I.-G., Udalski, A., Yee, J. C., et al. 2017, *AJ*, 154, 176
- Shin, I.-G., Udalski, A., Yee, J. C., et al. 2018, *ApJ*, 863, 23
- Shvartzvald, Y., Li, Z., Udalski, A., et al. 2016a, *ApJ*, 831, 183
- Shvartzvald, Y., Maoz, D., Udalski, A., et al. 2016b, *MNRAS*, 457, 4089
- Shvartzvald, Y., Udalski, A., Gould, A., et al. 2015, *ApJ*, 814, 111
- Shvartzvald, Y., Yee, J. C., Calchi Novati, S., et al. 2017, *ApJL*, 840, L3
- Skowron, J., Udalski, A., Kozłowski, S., et al. 2016, *AcA*, 66, 1
- Spergel, D., Gehrels, N., Breckinridge, J., et al. 2013, arXiv:1305.5422
- Street, R. A., Udalski, A., Calchi Novati, S., et al. 2016, *ApJ*, 819, 93
- Sumi, T., Bennett, D. P., Bond, I. A., et al. 2013, *ApJ*, 778, 150
- Sumi, T., Kamiya, K., Bennett, D. P., et al. 2011, *Natur*, 473, 349
- Suzuki, D., Bennett, D. P., Sumi, T., et al. 2016, *ApJ*, 833, 145
- Udalski, A. 2003, *AcA*, 53, 291
- Udalski, A., Han, C., Bozza, V., et al. 2018, *ApJ*, 853, 70
- Udalski, A., Szymański, M. K., & Szymański, G. 2015a, *AcA*, 65, 1
- Udalski, A., Yee, J. C., Gould, A., et al. 2015b, *ApJ*, 799, 237
- Wambsganss, J. 1997, *MNRAS*, 284, 172
- Wang, T., Zhu, W., Mao, S., et al. 2017, *ApJ*, 845, 129
- Wozniak, P. R. 2000, *AcA*, 50, 421
- Yee, J. C., Gould, A., Beichman, C., et al. 2015a, *ApJ*, 810, 155
- Yee, J. C., Shvartzvald, Y., Gal-Yam, A., et al. 2012, *ApJ*, 755, 102
- Yee, J. C., Udalski, A., Calchi Novati, S., et al. 2015b, *ApJ*, 802, 76
- Yoo, J., DePoy, D. L., Gal-Yam, A., et al. 2004, *ApJ*, 603, 139
- Zhu, W., Calchi Novati, S., Gould, A., et al. 2016, *ApJ*, 825, 60
- Zhu, W., Udalski, A., Calchi Novati, S., et al. 2017, *AJ*, 154, 210
- Zhu, W., Udalski, A., Gould, A., et al. 2015, *ApJ*, 805, 8